# Effects of Electric Field and Poling on the Cyclic Bending Fatigue in Cracked Piezoceramics

**Yasuhide Shindo[1,*], Fumio Narita[1], Masayuki Sato[1]**

[1] Department of Materials Processing, Graduate School of Engineering, Tohoku University, Sendai 980-8579, Japan
* Corresponding author: shindo@material.tohoku.ac.jp

**Abstract** We investigates the fatigue behavior of cracked piezoelectric ceramics in cyclic bending under electric fields both theoretically and experimentally. Fatigue tests were carried out in three-point bending with the single-edge precracked-beam (SEPB) specimens. The crack was created normal to the poling direction. Number of cycles to failure was measured under electric fields. Plane strain finite element analysis was also performed, and the effect of polarization switching on the energy release rate was discussed under high negative electric field. In addition, mechanisms for crack growth were discussed by scanning electron microscope examination of the fracture surface of the piezoelectric ceramics.

**Keywords** Piezomechanics, Finite element method, Material testing, PZT ceramics, Fatigue

## 1. Introduction

Research on fracture and fatigue of the lead zirconate titanate (PZT) ceramics has increased during the past decade. In recent years, the dynamic fatigue of SEPB hard PZT ceramics was studied under direct current (DC) electric field [1]. In the case under cyclic mechanical loading, Narita et al. [2] studied the fatigue crack growth in SEPB hard PZT ceramics under sinusoidal mechanical load and DC electric field, and discussed the effect of electric field on the crack growth rate versus maximum energy release rate curves.

It is expected that the polarization switching under high negative electric field affects the crack behavior of piezoelectric ceramics [3]. In particular, the polarizations are easy to switch in soft PZT ceramics, whereas hard PZT ceramics are very difficult to switch. Literature studies of fatigue in the PZT ceramics under high negative electric field are sparse and inconclusive. The main aim of this work is to discuss the effects of the electric field and polarization switching on the fatigue of cracked soft PZT ceramics in cyclic bending.

## 2. Experimental Procedure

Commercially supplied soft PZT C-91 ceramics (Fuji Ceramics Co. Ltd., Japan) were used. The material properties are listed in Table 1, and the coercive electric field is about $E_c$ = 0.35 MV/m. Fatigue tests under zero or negative electric fields were carried out using SEPB specimens. The specimen and testing set up are shown in Figure 1. PZT ceramics of 5 mm×5mm×5 mm were cut, and the specimen was produced by first poling a PZT and then bonding it between two unpoled PZTs. The size of the specimens was 5 mm thick, 5 mm wide, and 15 mm long. Vickers indents were introduced using the commercial microhardness testing machine. The specimens were compressed until a precrack was formed, and the crack has initial length of about 0.5 mm.

Three-point bending apparatus with 13 mm span was used, and load $P$ with constant-amplitude sinusoidal variation was applied with 250 N load cell (resolution : 0.01 N) to the specimens at constant frequency $f$ of 1 or 50 Hz. The load ratio, defined as the ratio of minimum load $P_{min}$ to maximum load $P_{max}$ of the fatigue cycle, was $R = P_{min}/P_{max} = 0.5$, and the maximum load $P_{max}$ was 90, 100 or 110 N. Number of cycles to failure under constant applied load $P_{max}$ and electric field was then measured. After the tests, scanning electron microscope (SEM) was used to examine

Table 1 Material properties of C-91

| Elastic compliance ($\times 10^{-12}$ m$^2$/N) | | | | | Piezoelectric constant ($\times 10^{-12}$m/V) | | | Dielectric permittivity ($\times 10^{-10}$ C/Vm) | |
|---|---|---|---|---|---|---|---|---|---|
| $s_{11}$ | $s_{33}$ | $s_{44}$ | $s_{12}$ | $s_{13}$ | $d_{31}$ | $d_{33}$ | $d_{15}$ | $\in_{11}^{T}$ | $\in_{33}^{T}$ |
| 17.1 | 18.6 | 41.4 | -6.3 | -7.3 | -340 | 645 | 836 | 395 | 490 |

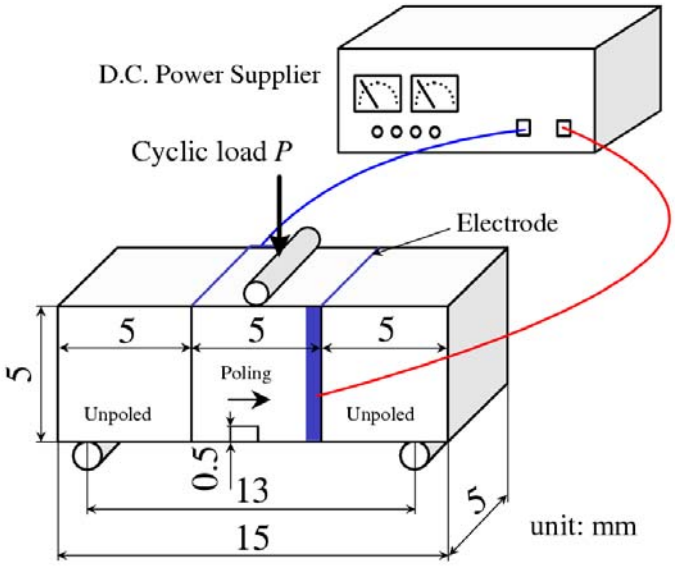


Figure 1. SEPB specimen and testing set up

fatigue fracture surfaces.

## 3. Analysis

Mechanical equilibrium and Gauss' law are given by

$$\sigma_{ji,j} = 0 \tag{1}$$

$$D_{i,i} = 0 \tag{2}$$

where $\sigma_{ij}$ and $D_i$ are the stress tensor and electric displacement vector, and a comma denotes partial differentiation with respect to the coordinates $x_i$ ($i$ = 1, 2, 3). We have employed Cartesian tensor notation and the summation convention for repeated tensor indices. In a ferroelectric material, domain switching leads to changes in remanent strain $\varepsilon_{ij}^{r}$ and remanent polarization $P_i^r$. Constitutive relations are described by

$$\varepsilon_{ij} = s_{ijkl}\sigma_{kl} + d_{kij}E_k + \varepsilon_{ij}^{r} \tag{3}$$

$$D_i = d_{ikl}\sigma_{kl} + \in_{ik}^{T} E_k + P_i^r \tag{4}$$

where $\varepsilon_{ij}$ and $E_i$ are the strain tensor and electric field vector, and $s_{ijkl}$, $d_{kij}$ and $\in_{ik}^{T}$ are the elastic compliance, direct piezoelectric constant and dielectric permittivity at constant stress, which satisfy the following symmetry relations:

$$s_{ijkl} = s_{jikl} = s_{ijlk} = s_{klij}\,, d_{kij} = d_{kji}\,, \in_{ij}^{T} = \in_{ji}^{T} \tag{5}$$

The strain and electric field may be expressed in terms of the displacement vector $u_i$ and the electric potential $\phi$ by

$$\varepsilon_{ij} = \frac{1}{2}(u_{j,i} + u_{i,j}) \tag{6}$$

$$E_i = -\phi_{,i} \tag{7}$$

The constitutive equations (3) and (4) for PZT poled in the $x_3$-direction are found in Appendix A.

The enhanced electromechanical field level results in localized polarization switching. When the electromechanical work exceeds a critical value, polarization switching occurs [4]. Thus the switching criterion is defined as

$$\sigma_{ij}\Delta\varepsilon_{ij} + E_i\Delta P_i \geq 2P^s E_c \tag{8}$$

where $P^s$ is spontaneous polarization, $E_c$ is coercive electric field, and $\Delta\varepsilon_{ij}$ and $\Delta P_i$ are the changes in the spontaneous strain $\gamma^s$ and spontaneous polarization during switching, respectively, and are given in Appendix B. The constitutive equations (3) and (4) after polarization switching are given by

$$\varepsilon_{ij} = s_{ijkl}\sigma_{kl} + d'_{kij}\,E_k + \varepsilon_{ij}^{r} \tag{9}$$

$$D_i = d'_{ikl}\,\sigma_{kl} + \in_{ik}^{T}\,E_k + P_i^{r} \tag{10}$$

where

$$d'_{ikl} = \{d_{33}n_i n_k n_l + d_{31}(n_i\delta_{kl} - n_i n_k n_l) + \frac{1}{2}d_{15}(\delta_{ik}n_l - 2n_i n_k n_l + \delta_{il}n_k)\} \tag{11}$$

In Eq. (11), $n_i$ is the unit vector in the poling direction and $\delta_{ij}$ is the Kroneker delta.

In order to evaluate the energy release rate $G$ of PZT, plane strain finite element analysis (FEA) was carried out for the cracked piezoelectric specimens under concentrated load $P$. The crack is assumed with faces normal (Case 1) or parallel (Case 2) to the polarization axis as shown in Fig.2. Let the coordinate axes $x = x_1$ and $z = x_3$ be chosen such that the $y = x_2$ axis coincides with the thickness direction. The $z$ axis is the poling direction. The three-point flexure specimen with span $S$ = 13 mm is the beam of width $W$ = 5 mm and length $L$ = 15 mm containing a crack of length $a$. The length between two electrodes is $L_0$ = 5 mm for Case 1 and $W$ = 5 mm for Case 2. Because of symmetry, only the half of the model was used in the FEA.

We first consider the Case 1 as shown in Fig. 2(a). The permeable crack model is treated, and the boundary conditions at $z$ = 0 can be expressed in the form

$$\begin{aligned} &u_z(x,0) = 0 \qquad (0 \leq x \leq W-a) \\ &\sigma_{zz}(x,0) = 0 \qquad (W-a < x \leq W) \end{aligned} \tag{12}$$

$$\sigma_{zx}(x,0) = 0 \qquad (0 \leq x \leq W) \tag{13}$$

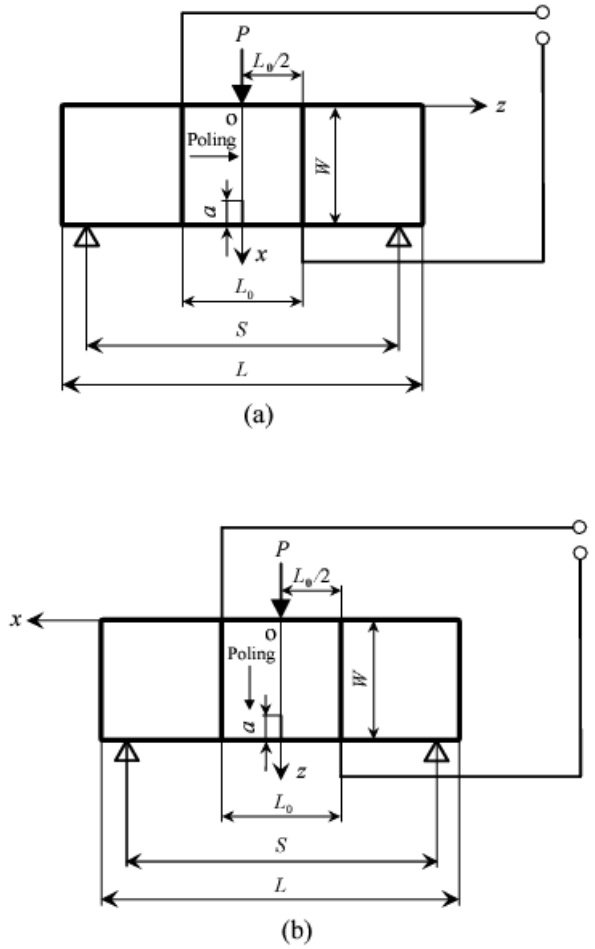


Figure 2. Schematic representation of the finite element model: (a) Case 1; (b) Case 2

$$\begin{aligned} &\phi(x,0) = 0 && (0 \le x \le W - a) \\ &E_x(x,0) = E_x^c(x,0) && (W - a < x \le W) \\ &D_z(x,0) = D_z^c(x,0) && (W - a < x \le W) \end{aligned} \tag{14}$$

where the superscript $c$ stands for the electric quantity in the void inside the crack. The electric potential is all zero on the symmetry planes inside the crack and ahead of the crack, so the boundary conditions of Eqs. (14) reduce to $\phi(x, 0) = 0$ ($0 \le x \le W$). Eqs. (14) are the permeable boundary conditions, and appropriate for a slit crack in piezoelectric ceramics [5]. Note that the fracture mechanics parameters such as energy release rate predicted by the permeable and discharging crack models are not significantly different, using the standard air breakdown field for a critical discharge level within the crack gap. A mechanical load is produced by the application of the prescribed force $P$, corresponding to the appropriate experimental load, at $x = 0$, $z = 0$ along the $x$-direction. For an electrical load, the electric potential ($\phi_0/2$) is applied at the edge $0 \le x \le W$, $z = L_0/2$, so the condition is

$$\phi(x, L_0/2) = (\phi_0/2) \qquad (0 \le x \le W) \tag{15}$$

The magnitude of the electric field $E_0$ in the $z$-direction is $-\phi_0/L_0$. Other boundary conditions are

summarized below.
At $z = L/2$ (side surface)

$$\sigma_{zz}(x, L/2) = 0 \qquad (0 \le x \le W) \tag{16}$$

$$\sigma_{zx}(x, L/2) = 0 \qquad (0 \le x \le W) \tag{17}$$

$$D_z(x, L/2) = 0 \qquad (0 \le x \le W) \tag{18}$$

At $x = 0$ (top surface)

$$\sigma_{xx}(0, z) = -(P/2)\delta(z) \qquad (0 \le z \le L/2) \tag{19}$$

$$\sigma_{xz}(0, z) = 0 \qquad (0 \le z \le L/2) \tag{20}$$

$$D_x(0, z) = 0 \qquad (0 \le z \le L/2) \tag{21}$$

At $x = W$ (bottom surface)

$$\sigma_{xx}(W, z) = 0 \quad (0 \le z < S/2, S/2 < z \le L/2), \quad u_x(W, S/2) = 0 \tag{22}$$

$$\sigma_{xz}(W, z) = 0 \qquad (0 \le z \le L/2) \tag{23}$$

$$D_x(W, z) = 0 \qquad (0 \le z \le L/2) \tag{24}$$

In Eq. (19), $\delta(\ )$ is the Dirac-delta function.

Next, we consider the Case 2 (see Figure 2(b)). The boundary conditions at $x = 0$ are

$$\begin{aligned} u_x(0, z) &= 0 \quad (0 \le z \le W - a) \\ \sigma_{xx}(0, z) &= 0 \quad (W - a < z \le W) \end{aligned} \tag{25}$$

$$\sigma_{xz}(0, z) = 0 \quad (0 \le z \le W) \tag{26}$$

$$\begin{aligned} \phi_{,x}(0, z) &= 0 \qquad (0 \le z \le W - a) \\ E_z(0, z) &= E_z^c(0, z) \quad (W - a < z \le W) \\ D_x(0, z) &= D_x^c(0, z) \quad (W - a < z \le W) \end{aligned} \tag{27}$$

The partial derivative of the electric potential with respect to $x$ is all zero on the symmetry planes inside the crack and ahead of the crack, so the boundary conditions of Eqs. (27) reduce to $\phi_{,x}(x, 0) = 0$ ($0 \le x \le W$). A mechanical load is produced by the application of the prescribed force $P$, at $x = 0$, $z = 0$ along the $z$-direction. For an electrical load, the electric potential $\phi_0$ is applied at the surface $0 \le x < L_0/2$, $z = W$, and the surface $0 \le x < L_0/2$, $z = 0$ is grounded, so the conditions are

$$\begin{aligned} &\phi(x,W) = \phi_0 \qquad (0 \le x < L_0/2) \\ &\phi(x,0) = 0 \qquad (0 \le x < L_0/2) \end{aligned} \tag{28}$$

The magnitude of the electric field $E_0$ in the $x$-direction is $-\phi_0/W$. Other boundary conditions are summarized below.
At $x = L/2$ (side surface)

$$\sigma_{xx}(L/2, z) = 0 \qquad (0 \le z \le W) \tag{29}$$

$$\sigma_{xz}(L/2, z) = 0 \qquad (0 \le z \le W) \tag{30}$$

$$D_x(L/2, z) = 0 \qquad (0 \le z \le W) \tag{31}$$

At $z = 0$ (top surface)

$$\sigma_{zz}(x,0) = -(P/2)\delta(x) \qquad (0 \le x \le L/2) \tag{32}$$

$$\sigma_{zx}(x,0) = 0 \qquad (0 \le x \le L/2) \tag{33}$$

$$D_z(x,0) = 0 \qquad (L_0/2 \le x \le L/2) \tag{34}$$

At $z = W$ (bottom surface)

$$\sigma_{zz}(x,W) = 0 \qquad (0 \le x < S/2, S/2 < x \le L/2), \qquad u_z(S/2,W) = 0 \tag{35}$$

$$\sigma_{zx}(x,W) = 0 \qquad (0 \le x \le L/2) \tag{36}$$

$$D_z(x,W) = 0 \qquad (L_0/2 \le x \le L/2) \tag{37}$$

In the FEA (ANSYS), the energy release rate was computed using the path-independent integral approach. The energy release rate $G$ for Case 1 is given by

$$G = \left(\int_{\Gamma_0} - \int_{\Gamma_p}\right)\{Hn_x - (\sigma_{xx}u_{x,x} + \sigma_{zx}u_{z,x})n_x - (\sigma_{zx}u_{x,x} + \sigma_{zz}u_{z,x})n_z + D_xE_xn_x + D_zE_xn_z\}d\Gamma \tag{38}$$

where $\Gamma_0$ is the contour closing the crack tip, $\Gamma_p$ is the path embracing that part of phase boundary which in enclosed by $\Gamma_0$, $H$ is the electrical enthalpy density, and $n_x$, $n_z$ are the components of the outer unit normal vector. The energy release rate $G$ for Case 2 is obtained by exchanging $x$ and $z$ in Eq. (38).

For the calculation of $G$, three contours were defined in the finite element mesh. The values of $G$ for each of these contours are practically identical. Four-node element PLANE 13 was used in the model. The finite element mesh had 4400 elements and 4536 nodes.

## 4. Results and Discussion

Table 2 shows the results of average number of cycles to failure (from two data) for PZT ceramics

Table 2 Number of cycles to failure under electric fields

| Electric field, $E_0$ (MV/m) | -0.2 | -0.04 | 0 |
|---|---|---|---|
| Number of cycles to failure, $N$ | 385 | 494645 | 38994 |

Table 3 Energy release rate under electric fields for Cases 1 and 2 without polarization switching effect

| Electric field, $E_0$ (MV/m) | | -0.2 | -0.04 | 0 |
|---|---|---|---|---|
| Energy release rate, $G$ (J/m$^2$) | Case 1 | 5.5 | 5.5 | 5.5 |
| | Case 2 | 4.3 | 4.3 | 4.3 |

C-91 under $P_{max}$ = 110 N ($R$ = 0.5, $f$ = 50 Hz) and $E_0$ = 0, -0.04, -0.2 MV/m. The value of average number of cycles to failure increases by about 12 times due to the electric field of -0.04 MV/m, but decreases to less than about 0.01 times due to the electric field of -0.2 MV/m. Although the results are not shown here, the fracture surface of the PZT ceramics under $E_0$ = 0 V/m shows intergranular and transgranular regions, and the micrograph of the PZT ceramics under $E_0$ = -0.04 MV/m reveals a predominantly intergranular fracture. On the other hand, crack paths in the fracture for PZT ceramics under $E_0$ = -0.2 MV/m are predominantly transgrannular.

Table 3 lists the energy release rate $G$ for SEPB C-91 ceramics with a crack of length $a$ = 0.5 mm under load $P_{max}$ = 110 N and $E_0$ = 0, -0.04, -0.2 MV/m for Cases 1 and 2 without polarization switching effect. The energy release rates for Cases 1 and 2 are independent of the electric field,

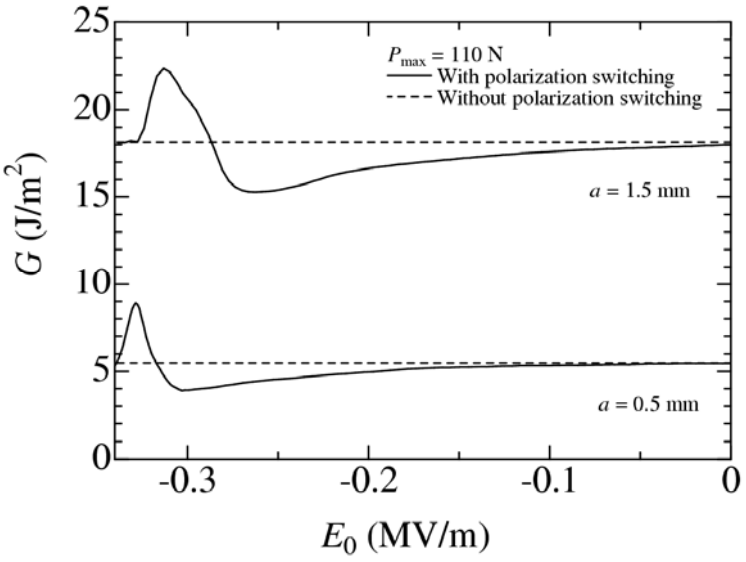


Figure 3. Energy release rate vs electric field for Case 1 with and without polarization switching effect

and the energy release rate for Case 1 is larger than that for Case 2. Figure 3 shows the energy release rate $G$ versus electric field $E_0$ for SEPB C-91 ceramics with $a$ = 0.5 and 1.5 mm under $P_{max}$ = 110 N for Case 1. The dashed line represents the value of $G$ without polarization switching effect, and the solid line represents the $G$ with switching effect. The prediction with switching effect shows that localized polarization switching leads to a decrease in $G$ and then an increase after $E_0$ reaches about -0.3 and -0.27 MV/m for $a$ = 0.5 and 1.5 mm, respectively.

In concluding, numbers of cycles to failure under low and high negative electric fields were significantly larger and smaller than that under zero electric field, and correlated with the fracture surfaces. In addition, as the negative electric field increased, the localized polarization switching led to a decrease in the energy release rate, and the energy release rate increased when the negative electric field increased further.

**References**

[1] Y.Shindo, F.Narita, M.Hirama, Dynamic fatigue of cracked piezoelectric ceramics under electromechanical loading: Three-point bending test and finite element analysis. J Mech Mater Struct, 4 (2009) 719-729.
[2] F.Narita, Y.Shindo, F.Saito, Cyclic Fatigue Crack Growth in Three-Point Bending PZT Ceramics under Electromechanical Loading. J Am Ceram Soc, 90 (2007) 2517-2524.
[3] Y.Shindo, F.Narita, T.Matsuda, Electric field dependence of the mode I energy release rate in single-edge cracked piezoelectric ceramics: Effect due to polarization switching/dielectric breakdown. Acta Mech, 219 (2011) 129-143.
[4] S.C.Hwang, C.S.Lynch, R.M.McMeeking, Ferroelectric/ferroelastic interactions and a polarization switching model. Acta Metall Mater, 43 (1995) 2073-2084.
[5] Y.Shindo, F.Narita, M.Hirama, Effect of the electrical boundary condition at the crack face on the mode I energy release rate in piezoelectric ceramics. Appl Phys Lett, 94 (2009) 081902.
[6] Y.Shindo, M.Yoshida, F.Narita, K.Horiguchi, Electroelastic field concentrations ahead of electrodes in multilayer piezoelectric actuators: experiment and finite element simulation. J Mech Phys Solids, 52 (2004) 1109-1124.

## Appendix A

For piezoelectric ceramics which exhibit symmetry of a hexagonal crystal of class 6 mm with respect to principal $x_1$, $x_2$ and $x_3$ axes, the constitutive relations can be written in the following form:

$$\begin{Bmatrix} \varepsilon_{11} \\ \varepsilon_{22} \\ \varepsilon_{33} \\ \varepsilon_{23} \\ \varepsilon_{31} \\ \varepsilon_{12} \end{Bmatrix} = \begin{bmatrix} s_{11} & s_{12} & s_{13} & 0 & 0 & 0 \\ s_{12} & s_{11} & s_{13} & 0 & 0 & 0 \\ s_{13} & s_{13} & s_{33} & 0 & 0 & 0 \\ 0 & 0 & 0 & s_{44}/2 & 0 & 0 \\ 0 & 0 & 0 & 0 & s_{44}/2 & 0 \\ 0 & 0 & 0 & 0 & 0 & s_{66}/2 \end{bmatrix} \begin{Bmatrix} \sigma_{11} \\ \sigma_{22} \\ \sigma_{33} \\ \sigma_{23} \\ \sigma_{31} \\ \sigma_{12} \end{Bmatrix} + \begin{bmatrix} 0 & 0 & d_{31} \\ 0 & 0 & d_{31} \\ 0 & 0 & d_{33} \\ 0 & d_{15}/2 & 0 \\ d_{15}/2 & 0 & 0 \\ 0 & 0 & 0 \end{bmatrix} \begin{Bmatrix} E_1 \\ E_2 \\ E_3 \end{Bmatrix} + \begin{Bmatrix} \varepsilon_{11}^r \\ \varepsilon_{22}^r \\ \varepsilon_{33}^r \\ \varepsilon_{23}^r \\ \varepsilon_{31}^r \\ \varepsilon_{12}^r \end{Bmatrix} \tag{A.1}$$

$$\begin{Bmatrix} D_1 \\ D_2 \\ D_3 \end{Bmatrix} = \begin{bmatrix} 0 & 0 & 0 & 0 & d_{15} & 0 \\ 0 & 0 & 0 & d_{15} & 0 & 0 \\ d_{31} & d_{31} & d_{33} & 0 & 0 & 0 \end{bmatrix} \begin{Bmatrix} \sigma_{11} \\ \sigma_{22} \\ \sigma_{33} \\ \sigma_{23} \\ \sigma_{31} \\ \sigma_{12} \end{Bmatrix} + \begin{bmatrix} \in_{11}^{\mathrm{T}} & 0 & 0 \\ 0 & \in_{11}^{\mathrm{T}} & 0 \\ 0 & 0 & \in_{33}^{\mathrm{T}} \end{bmatrix} \begin{Bmatrix} E_1 \\ E_2 \\ E_3 \end{Bmatrix} + \begin{Bmatrix} P_1^r \\ P_2^r \\ P_3^r \end{Bmatrix} \tag{A.2}$$

where

$$\sigma_{23} = \sigma_{32}, \quad \sigma_{31} = \sigma_{13}, \quad \sigma_{12} = \sigma_{21} \tag{A.3}$$

$$\varepsilon_{23} = \varepsilon_{32}, \quad \varepsilon_{31} = \varepsilon_{13}, \quad \varepsilon_{12} = \varepsilon_{21} \tag{A.4}$$

$$\varepsilon_{23}^r = \varepsilon_{32}^r, \quad \varepsilon_{31}^r = \varepsilon_{13}^r, \quad \varepsilon_{12}^r = \varepsilon_{21}^r \tag{A.5}$$

$$\begin{aligned} &s_{11} = s_{1111} = s_{2222}, \quad s_{12} = s_{1122}, \quad s_{13} = s_{1133} = s_{2233}, \quad s_{33} = s_{3333}, \\ &s_{44} = 4s_{2323} = 4s_{3131}, \quad s_{66} = 4s_{1212} = 2(s_{11} - s_{12}) \end{aligned} \tag{A.6}$$

$$d_{15} = 2d_{131} = 2d_{223}, \quad d_{31} = d_{311} = d_{322}, \quad d_{33} = d_{333} \tag{A.7}$$

## Appendix B

The values of $\Delta\varepsilon_{ij} = \varepsilon_{ij}^r$ and $\Delta P_i = P_i^r$ for 180° switching can be expressed as

$$\Delta\varepsilon_{11} = 0, \quad \Delta\varepsilon_{22} = 0, \quad \Delta\varepsilon_{33} = 0, \quad \Delta\varepsilon_{12} = 0, \quad \Delta\varepsilon_{23} = 0, \quad \Delta\varepsilon_{31} = 0 \tag{B.1}$$

$$\Delta P_1 = 0, \quad \Delta P_2 = 0, \quad \Delta P_3 = -2P^s \tag{B.2}$$

For 90° switching in the $x_3x_1$ plane, the changes are

$$\Delta\varepsilon_{11} = \gamma^s, \quad \Delta\varepsilon_{22} = 0, \quad \Delta\varepsilon_{33} = -\gamma^s, \quad \Delta\varepsilon_{12} = 0, \quad \Delta\varepsilon_{23} = 0, \quad \Delta\varepsilon_{31} = 0 \tag{B.3}$$

$$\Delta P_1 = \pm P^s, \quad \Delta P_2 = 0, \quad \Delta P_3 = -P^s \tag{B.4}$$

For 90° switching in the $x_2x_3$ plane, we have

$$\Delta\varepsilon_{11} = 0, \quad \Delta\varepsilon_{22} = \gamma^s, \quad \Delta\varepsilon_{33} = -\gamma^s, \quad \Delta\varepsilon_{12} = 0, \quad \Delta\varepsilon_{23} = 0, \quad \Delta\varepsilon_{31} = 0 \tag{B.5}$$

$$\Delta P_1 = 0, \quad \Delta P_2 = \pm P^s, \quad \Delta P_3 = -P^s \tag{B.6}$$